Topological band gaps and edge modes materialized by symmetric silicon-on-insulator photonic crystal slabs in the mid-IR range

Afshan Begum [1,2,*] Yuanzhao Yao [3,*,†] Takashi Kuroda [3] Yoshihiko Takeda [1,2] Naoki Ikeda [4]
Yoshimasa Sugimoto [3] Takaaki Mano [3] and Kazuaki Sakoda [3,‡]

[1]*Center for Green Research on Energy and Environmental Materials, National Institute for Materials Science, Tsukuba 305-0003, Japan*
[2]*Doctoral Program in Materials Science and Engineering, University of Tsukuba, Tsukuba 305-8577, Japan*
[3]*Research Center for Functional Materials, National Institute for Materials Science, Tsukuba 305-0044, Japan*
[4]*Research Network and Facility Service Division, National Institute for Materials Science, Tsukuba 305-0047, Japan*

We successfully fabricated silicon-on-insulator (SOI) photonic crystal (PhC) slabs in which electromagnetic topological band gaps and edge modes were materialized for symmetric transverse-electric-like modes. Because the structure of our specimens can be regarded as symmetric about the horizontal middle plane of the PhC slab, their symmetric and antisymmetric eigenmodes were rigorously separated, so we could achieve genuine photonic band gaps for the former. We fabricated those specimens by electron beam lithography of the top Si layer of SOI wafers and successive plasma-enhanced chemical vapor deposition of a SiO_2 capping layer. We confirmed the complete common band gap of topologically trivial and nontrivial PhCs and the topological edge modes on the boundary between them by angle-resolved reflection spectroscopy in the mid-infrared range. This is an observation of the common band gap and edge modes that materialized in symmetric PhC slabs without a membrane structure, that is, without the etching of a sacrificial layer under the PhC to increase the refractive-index contrast and the width of the common band gap.

I. INTRODUCTION

Topological edge modes in the electromagnetic spectrum, which imitate the quantum spin Hall effect [1–5], have introduced a novel principle of wave confinement and propagation and may serve as new building blocks for optical microcircuits [6–11]. They are materialized on the boundary between topologically trivial and nontrivial photonic crystals (PhCs), for which Wu and Hu reported the design based on the C_{6v}-symmetric PhC structure [6]. The trivial and nontrivial band gaps are created for transverse magnetic (TM) modes between E_1 (dipole)-symmetric and E_2 (quadruple)-symmetric eigenmodes on the Γ point of the first Brillouin zone according to the order of their frequencies, which can be controlled by structural parameters of the PhC unit cell. Their idea stimulated many researchers to promote the investigation of the topological edge modes to mitigate disorder-induced backscattering and exploit directional control of light.

The limited extent of topological protection and the backscattering of the edge modes have been reported for both topological insulators [12–15] and topological PhCs [16]. In addition, we must bear in mind that the practical photonic systems are non-Hermitian. Most of the surface modes of two-dimensional PhC thin films, which are called PhC slabs, suffer from the diffraction loss and have a finite lifetime,

which is another origin of the limited topological protection. On the other hand, the photonic system has its own merits. For example, sample fabrication is relatively flexible, and we can introduce defect structures of any shapes by simply changing the design drawing (CAD data) for lithography, so we can imitate and examine some of the problems in the quantum spin Hall effect and new classes of material systems proposed by *topological quantum chemistry* [17,18]. Another merit is a direct access to the edge modes with incident light waves using non-Hermiticity.

Barik *et al.* extended the original design for purely two-dimensional PhCs to PhC membranes by changing the shape of the dielectric materials composing the unit cell [7,8]. Specifically, they adapted a triangular shape of air cylinders for their PhC membranes to prevent the band gap from closing on the M point. Thus, they proved the presence of complete band gaps for transverse-electric (TE)-like modes common to the trivial and nontrivial PhC membranes, which resulted in the presence of the edge modes, by both theory and experiment.

However, the membrane or air-bridged structure needs a sacrificial layer beneath the PhC layer, which should be removed by selective etching after the PhC layer is fabricated [7–11,19–29]. The PhC membranes generally have large photonic band gaps due to the large refractive-index contrast between air and dielectric materials consisting of the unit cell. Because the common band gap, which is defined as the band-gap frequency range shared by two PhCs, is a prerequisite for the topological edge modes, its large value is desirable for practical experimental studies. For example, complete common band gaps of 4.1% and 4.7% widths relative to the

---
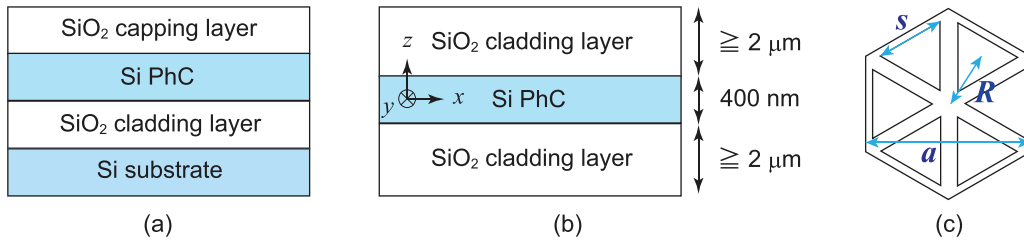
FIG. 1. Design of the symmetric SOI PhC. (a) Side view of the SOI PhC with a SiO$_2$ capping layer. (b) Side view of the symmetric Si PhC slab. The *x-y* plane is taken at the middle of the Si PhC slab. (c) Top view of the unit cell of the Si PhC, which consists of six triangular holes arranged in the C$_{6v}$ symmetry. In the numerical calculation, the lattice constant *a*, the side length *s*, and the thickness of the Si PhC layer were fixed to 2 μm, 800 nm, and 400 nm, respectively. The distance between the center of the unit cell and the center of the triangular hole, *R*, was varied from 620 to 700 nm.

mid-gap frequency were reported in Refs. [8,9], respectively. However, their mother materials are limited, their fabrication process is complicated, and their mechanical strength is low, while the PhC membranes have particular applications such as cavity optomechanics [30,31].

Here, we report on the design and fabrication of non-air-bridged PhC slabs to materialize a complete common band gap for the symmetric TE-like modes and topological edge modes. Specifically, we propose PhC slabs consisting of Si PhC sandwiched by two SiO$_2$ layers, which can be regarded as symmetric about the horizontal middle plane of the Si PhC so that the lowest-order symmetric TE-like modes and the lowest-order antisymmetric TM-like modes are separated rigorously and genuine band gaps are obtained for the former. We show that we can materialize the complete common band gap of a 4.1% width relative to the mid-gap frequency. We prove the presence of the complete common band gap and the edge modes by specimen fabrication on SOI (silicon-on insulator) wafers and evaluation by angle-resolved reflection spectroscopy.

This paper is organized as follows. In Sec. II, we show our sample design by the finite element method (FEM) calculations. Specimen fabrication is described in Sec. III. The method for the angle-resolved reflection measurements is explained in Sec. IV. We describe the results of the measurements in Sec. V and give a brief conclusion in Sec. VI. To prove the negligibly small influence of the Si substrate of the SOI wafer on the electromagnetic eigenmodes in the frequency range of our interest, the comparison of dispersion curves between SiO$_2$ under layers with finite and infinite thicknesses is presented in the Appendix.

II. SAMPLE DESIGN

We followed the recipe by Barik *et al.* [7,8] for the sample design. We examined the triangular lattice of air holes fabricated in the top Si layer of SOI wafers. In their original design, they analyzed and fabricated PhC membranes by selective etching of a sacrificial layer under a GaAs PhC. The membrane structures have a large refractive-index contrast, so they are generally advantageous for creating large photonic band gaps, while their fabrication is complicated, and their mechanical strength is low. Another merit of the membrane PhC is that the symmetric and antisymmetric modes are rigorously defined since their structure can safely be regarded

as symmetric about the horizontal middle plane of the PhC [32]. So, we can discuss the presence of the well-defined photonic band gap in each case separately.

In this study, we tried to find a non-air-bridged specimen design that does not need the underetching and yet it can be regarded as symmetric about the horizontal middle plane. For this purpose, we examined Si PhCs sandwiched by SiO$_2$ layers as shown in Fig. 1(a). The thickness of the top Si layer and the SiO$_2$ layer below it was fixed at 400 nm and 3 μm, respectively, according to available SOI wafers (SOITEC). As we show in the Appendix, when the thickness of the SiO$_2$ layer is larger than 2 μm, the dispersion relation of the electromagnetic eigenmodes confined in the top Si layer is practically the same as in the case of an infinitely thick SiO$_2$ layer in the frequency range of our interest, that is, 2 μm (5000 cm^{-1}) to 4 μm (2500 cm^{-1}). So, the sandwiched structure of Fig. 1(a) can safely be regarded as symmetric about the horizontal middle plane located in the Si PhC as shown in Fig. 1(b) when the SiO$_2$ capping layer is also thicker than 2 μm. The triangular air holes fabricated in the top Si layer by lithography will be filled with SiO$_2$ during the chemical vapor deposition (CVD) growth process of the capping layer, so we assumed the refractive index of SiO$_2$ for this region in the FEM numerical calculations.

The solid and broken lines in Fig. 2 show the dispersion relation of two symmetric PhCs calculated by FEM with COMSOL Multiphysics, whereas the circles and triangles denote eigenfrequencies observed by angle-resolved reflection spectroscopy, which will be described in Sec. V. For the numerical calculation, we located a perfectly matched layer (PML) absorbing boundary at $z = 6$ μm in the SiO$_2$ capping layer and assumed a symmetric boundary condition for the electric field at $z = 0$ μm (the horizontal middle plane of the Si PhC layer). Because the PML absorbing boundary is located sufficiently far from the Si layer compared with the localization length in the z direction, this condition is equivalent to an infinitely thick SiO$_2$ layer. The latter condition excludes the antisymmetric modes, and we can selectively calculate the symmetric modes.

Figures 2(a) and 2(b) show the dispersion relation of specimens named PhC-t and PhC-n, respectively, whose structural parameters are given in the figure caption. The dispersion curves are plotted in the Γ-to-K and Γ-to-M directions in the first Brillouin zone. Because the PhC structure is highly symmetric (C$_{6v}$), there are polarization selection rules for
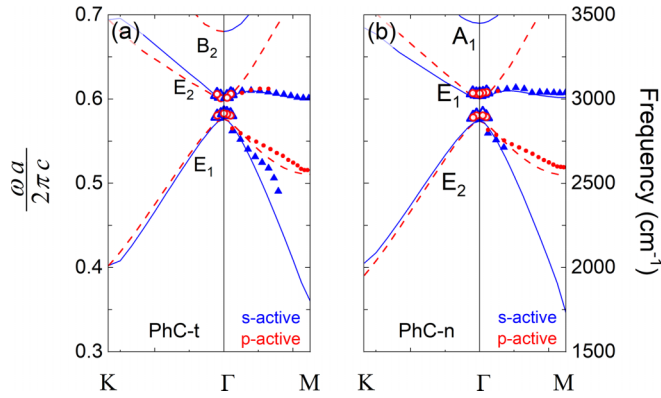
FIG. 2. Dispersion relation of (a) PhC-t and (b) PhC-n. The horizontal axis is the wave vector in the first Brillouin zone, and the vertical axes are genuine (right) and normalized (left) frequencies, where ω, a, and c are the angular frequency, the lattice constant, and the light velocity in free space, respectively. The red broken lines and blue solid lines denote p- and s-active symmetric modes, respectively, calculated by FEM. The red open circles and blue open triangles denote eigenfrequencies acquired by our homemade high-resolution setup, whereas the red solid circles and blue solid triangles show those measured by Seagull. Designed structural parameters are as follows: $a = 2.0$ μm, $s = 800$ nm, $R = 620$ nm for PhC-t, and $R = 700$ nm for PhC-n. The refractive indices of Si and SiO$_2$ were assumed to be 3.427 [33] and 1.440 [34], respectively, in the numerical calculations.

eigenmodes propagating in these directions [35]. The blue solid lines and the red broken lines in Fig. 2 represent eigenmodes active to s and p polarizations, respectively. E_1, E_2, A_1, and B_2 denote the symmetry of the magnetic field of eigenmodes on the Γ point, which was clarified by examining their field distribution obtained by numerical calculations.

It is evident that there is a complete band gap between the E_1 and E_2 modes for the two PhCs. Because the E_1-mode frequency is lower (higher) than the E_2-mode frequency for PhC-t (PhC-n), the band gap is topologically trivial (nontrivial) [6]. In addition, Fig. 2 clearly shows that we can materialize a complete band gap common to the trivial and nontrivial PhCs, so we can also materialize helical edge modes on the boundary between the two PhCs [6]. The common band gap is 4.1% wide relative to the mid-gap frequency. Surprisingly, this relative width was comparable to the case of PhC membranes, 4.1% in Ref. [8] and 4.7% in Ref. [9], for example, in spite of the relatively small refractive-index contrast. This is because the band gap is not only dependent on the refractive-index contrast but also dependent on the degree of symmetry breaking described by R, since the band gap vanishes for the symmetric case of the honeycomb lattice.

Next, we calculated the topological edge modes localized on the boundary between the two PhCs. We assumed PhC-n and PhC-t of 11 unit cells in positive and negative y regions, respectively, as shown in Fig. 3(a) and set the PML absorbing boundary on both ends. The red broken line denotes the unit structure, on which the Bloch boundary condition was imposed in the x direction. As Fig. 3(b) shows, helical edge modes are materialized in the band-gap frequency range accompanied by a small gap on the Γ point due to the lack
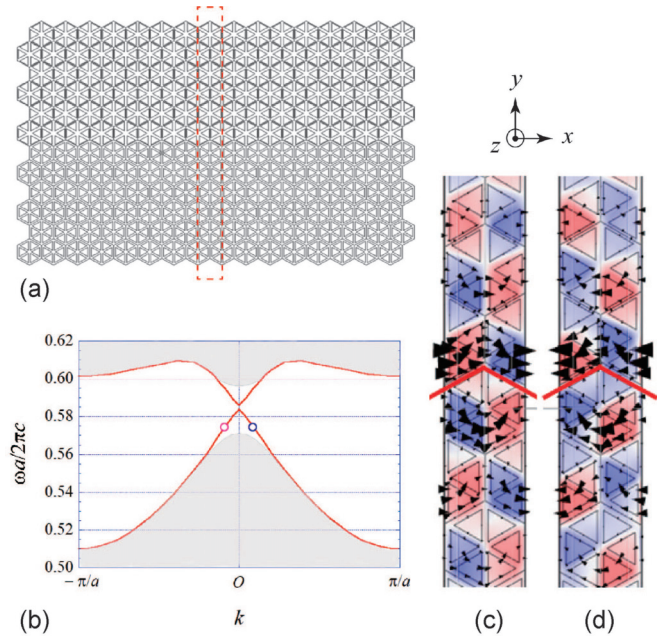
FIG. 3. (a) Geometry for materializing topological edge modes using the symmetric SOI-PhCs. The upper half is a topologically nontrivial PhC (PhC-n), whereas the lower half is a topologically trivial PhC (PhC-t). The edge modes are materialized on their boundary. The red broken line denotes the unit structure, on which the Bloch boundary condition was imposed in the x direction, whereas the PML absorbing boundary condition was imposed in the other two directions. (b) Red solid line: Dispersion relation of topological edge modes materialized on the boundary between the two PhCs. Gray region: Frequency ranges of bulk modes. The vertical axis is the normalized frequency and the horizontal axis is the wave vector in the x direction. Red and blue circles: Eigenmodes whose field distributions and Poynting's vectors are presented in panels (c) and (d), respectively. The field distributions and Poynting's vectors are for the (c) right-going and (d) left-going edge modes. Black wedges show the direction and magnitude of the Poynting's vectors. Blue and red colors show the positive and negative magnetic fields in the vertical (z) direction. The bent red lines denote the boundary between the two PhCs.

of the inversion symmetry caused by the PhC boundary. The two split modes on the Γ point are linearly polarized due to the 1:1 mixture of the two helical modes with right circular and left circular polarizations. Calculated far-field patterns showed that the lower and upper branches are polarized in the x and y directions, respectively. When we move away from the Γ point, this mixture diminishes, and the helical edge modes go back to their original character of the circular polarization. Because the dispersion curves of the edge modes are located above the light line, their lifetime is finite due to the diffraction loss [32]. The quality factor, which is defined by the ratio of the real part of the eigenfrequency to two times its imaginary part, is approximately 300 for both upper and lower branches on the Γ point. A typical localization length in the y direction was 3.9 a, which was obtained by curve fitting to the distribution of the magnetic field intensity calculated for the edge modes denoted by the circles in Fig. 3(b), whose field distributions and Poynting's vectors are shown in Figs. 3(c)
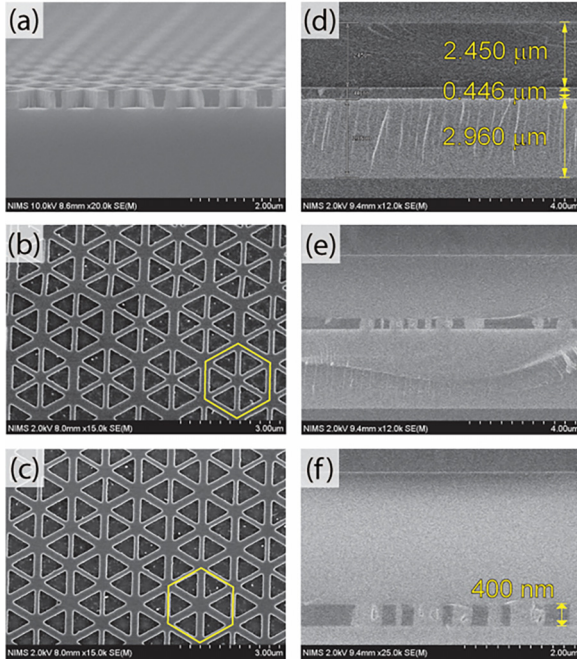
FIG. 4. Scanning electron microscopy (SEM) images of the fabricated specimens. (a) Cross-sectional view of the specimen after etching. The nanostructure obtained has smooth walls. (b) Top-view SEM of PhC-t with $R = 620$ nm and (c) PhC-n with $R = 700$ nm. (d) Cross-sectional SEM of the specimen after growing the SiO$_2$ capping layer. (e) Cross-sectional view of PhC walls buried in the SiO$_2$. (f) Close-up of the PhC walls, showing minimal void formation.

FIG. 5. Normal incidence reflection spectra of PhC-t measured by the IR microscope (a) before and (b) after growing the SiO$_2$ capping layer (black solid line) and calculated spectra (blue dotted line). The red arrows mark the calculated E_1-mode frequencies. In panel (a), the upper and lower limits of the reflection spectra are 1 and 0, respectively. Spectra in panel (b) are drawn in the same scale and shifted by 1 in the vertical direction.

and 3(d). The localization length was comparable to the case of asymmetric SOI-PhCs in our previous study, 3.6 a [36].

III. SAMPLE FABRICATION

We fabricated the specimens by standard electron beam lithography (Elionix, ELS-125) of SOI wafers (SOITEC) with high-contrast e-beam resist (Allresist, AR-P6200) and exposure parameters of an accelerating voltage of 125 kV, a current of 1 nA, a field size of 250 µm, 50 000 dot numbers, and a shot time of 0.06 µs/dot of 240 µC/cm^2 dose. The pattern was developed at room temperature in xylene for 90 s, followed by isopropyl alcohol (IPA) wash for 30 s with slow puddling. Then we performed the through etching of 400 nm in depth using the deep reactive ion etching Bosch process with 27 cycles, having an etch rate of 15.14 nm/cycle. The residue resist was removed by a 20-min dip in 80 °C organic solvent NMP (N-methyl-2-pyrrolidone), followed by an acetone wash, an IPA wash, and plasma ashing. Figure 4(a) is a cross-sectional scanning electron microscopy (SEM) image of one of the samples at this stage, showing the acquired smooth vertically etched walls.

We fabricated 3 mm by 3 mm photonic crystal slabs of the trivial (PhC-t) and nontrivial (PhC-n) bulk samples. The top view of the PhCs is presented in Figs. 4(b) and 4(c), respectively, revealing sharp vertices of the triangular holes and consistent side lengths s that were achieved in the fabrication.

These sharp vertices are essential to open the band gap for symmetric TE-like modes [7,8].

The samples were then capped with a 2.45-µm-thick SiO$_2$ by plasma-enhanced chemical vapor deposition (PECVD) using a combination of tetraethyl orthosilicate (TEOS) [or Si(OC$_2$H$_5$)$_4$] in the presence of oxygen (O$_2$). We used TEOS at a flow rate of 5 sccm, under 195 sccm of O$_2$, and applying 50 W of radio-frequency power. We deposited SiO$_2$ for 62 min, at a rate of 40 nm/min. The substrate holder was maintained at a temperature of 350 °C throughout the deposition. Figure 4(d) shows the cross-sectional SEM of the SOI wafer having a 3-µm insulating layer, a silicon layer of 0.4 µm, and a chemically grown SiO$_2$ layer of 2.45 µm. Figures 4(e) and 4(f) are the cross sections of PhCs buried in SiO$_2$ and an enlarged view, respectively. The SEM pictures show a small number of air voids. We estimated their volume percentage by comparing calculated and observed E_1-mode frequencies. Because their agreement is quite good for both uncapped and capped specimens (see Fig. 5), the CVD process was satisfactory. We estimated from the small discrepancy in the E_1-mode frequencies that the volume percentage of the air voids was smaller than 1%.

In the same manner, we fabricated another sample that consisted of repetitive arrays of zig-zag boundaries between the trivial and nontrivial PhCs, which we hereafter call the combination specimen. Each zig-zag boundary is made up of 20 unit cells of trivial and nontrivial PhCs on either side.

IV. MEASUREMENTS

Angle-resolved reflection spectra in the mid-IR range were measured in the same manner as in our previous studies [35–38]. We used a Fourier-transform (FT)-IR spectrometer (JASCO, FT/IR-6800) with a 2.0-cm^{-1} spectral resolution. For the reflection measurement around the Γ point of the first Brillouin zone, we used our homemade optical setup to materialize a 0.3° angle resolution [39], which was integrated in the sample chamber of the FT-IR spectrometer, while we used a commercial attachment, Seagull (Harrick Scientific), for 5° to 70° incident angles. For polarization-dependent measurements, we used a nanoparticle-film polarizer. The measured reflectance was normalized by using that of a silver mirror.

We also used an IR microscope (JASCO, IRT-5200) for the normal-incidence reflection measurements. For the collection of the reflected light, we attached a CaF$_2$ singlet lens with a focusing length of 50 mm (Thorlabs, LA5763) together with an iris with a diameter of approximately 5 mm to the microscope. The setup made it possible to measure near-normal incidence spectra with an angle resolution of approximately 5°.

V. RESULTS AND DISCUSSION

A. Bulk modes

Figure 5 shows the reflection spectra of PhC-t measured by the IR microscope at normal incidence (a) before and (b) after growing the SiO$_2$ capping layer (black solid line). Their fundamental features agree very well with calculated spectra (blue dotted line). In each panel, a big Fano-type resonance peak originating from the E_1 mode is superimposed on smooth undulations caused by the interference of the Si and SiO$_2$ multilayers in the SOI wafer. The resonance frequencies agree quite well with calculated E_1-mode frequencies, which are denoted by red arrows. Their discrepancy was smaller than 0.22%. In Fig. 5, there is another small resonance around 3240 cm^{-1} in panel (a) and around 3010 cm^{-1} in panel (b) that is caused by the E_2 mode on the Γ point. The E_2 (quadruple) mode is originally inactive to the incident light from the normal direction [35]. However, the angle resolution of the IR microscope was not high ($\approx 5°$), and so eigenmodes of small but nonzero wave vectors were weakly detected at this frequency. The spectral features were shifted to lower frequencies by growing the capping layer because of the increase in the refractive index. The excellent agreement between the measured and calculated spectra is evidence for the accuracy of our calculations and sample fabrication.

To evaluate the dispersion relation around the Γ point, we examined the angle-resolved reflection spectra in the Γ-to-K and Γ-to-M directions for both s and p polarizations. Figure 6 shows the spectra of (a) PhC-t and (b) PhC-n measured by our homemade high-resolution setup. The incident angle was tuned from $\theta = -3.79°$ to 3.79°. Each panel in Fig. 6 consists of 27 reflection spectra measured in 0.292° steps. The upper and lower limits of the lowest reflection spectrum are 1 and 0, respectively. Other spectra are drawn in the same scale and shifted by 0.15 in the vertical direction.

In each spectrum, one or two sharp peaks of the Fano-type resonance are superimposed on the smooth background undulations. The sharp Fano-type peaks originate from the PhC

eigenmodes; therefore, their dispersion relation can be obtained by plotting the resonance frequency against the lateral wave-vector component of the incident light. Each resonance frequency was estimated by curve fitting to the observed spectrum with a combination of an asymmetric Lorentzian function (Fano function) for the PhC eigenmode and a third-order polynomial function for the background undulation. Because the spectra for the s and p polarizations are close to each other, we can conclude that the relevant eigenmodes are doubly degenerate on the Γ point; that is, they are the E_1 mode or the E_2 mode. In addition, from the fact that the smaller peak disappears at $\theta = 0°$ while the bigger peak does not, we can conclude that the former is the E_2 mode and the latter is the E_1 mode according to the selection rules [35]. Because the E_2-mode (E_1-mode) frequency is higher for PhC-t (PhC-n), its band gap is a trivial (nontrivial) one [6].

The data points thus obtained are plotted (open circle and triangle) around the Γ point in Fig. 2, whose frequencies are very close to the calculated dispersion curves. In fact, E_1- and E_2-mode frequencies were 2915.8 and 3009.6 cm^{-1} (measured) and 2882.4 and 3002.7 cm^{-1} (calculated) for PhC-t, and 3029.5 and 2917.0 cm^{-1} (measured) and 3002.5 and 2871.2 cm^{-1} (calculated) for PhC-n. Their discrepancy was smaller than 1.6% and 28.3 cm^{-1} on average, which is again evidence for the accuracy of our calculation and sample fabrication. Note that the E_2-mode peak disappears on the Γ point ($\theta = 0°$), so we estimated its frequency by curve fitting with a quadratic function to the observed dispersion data for nonzero wave vectors.

To examine whether these band gaps are complete gaps, we measured reflection spectra for larger incident angles ($\theta = 5°–70°$) with Seagull in the Γ-to-M direction, since the band gap does not decrease but rather increases in the Γ-to-K direction, so a possible gap closing takes place only in the Γ-to-M direction. The measured reflection spectra are presented in Fig. 7, in which systematic shifts of Fano-type resonance peaks are clearly observed with increasing incident angle. The spectral width of the Fano-type resonance peaks is generally larger than that of Fig. 6, mainly because the angle resolution of our homemade setup is better than that of Seagull. For the reflection spectra in Fig. 7, the resonance frequency was estimated by the average of the local minimum and maximum frequencies of each Fano-type peak. Their data points are also plotted (solid circles and triangles) in Fig. 2. We can clearly see that the photonic band gap found around the Γ point is kept open all the way to the M point. Actually, the measured frequency of the upper s-active mode on the M point was 3005.0 cm^{-1} for PhC-t and 3056.1 cm^{-1} for PhC-n. These values are higher than the upper gap-edge frequency on the Γ point; therefore, the band-gap frequency range is defined by the E_1 and E_2 modes on the Γ point. Thus, we confirmed the complete band gap of the symmetric TE-like modes for both PhC-t and PhC-n.

In addition, Fig. 2 clearly shows that PhC-t and PhC-n share a common complete band gap, which is a prerequisite for topological edge modes, from 2917.0 to 3009.6 cm^{-1} experimentally and 2882.4 to 3002.5 cm^{-1} theoretically. This gives us a band gap of 3.1% common to both PhC-t and PhC-n experimentally. So, we can expect the presence of the edge modes localized on the boundary between the
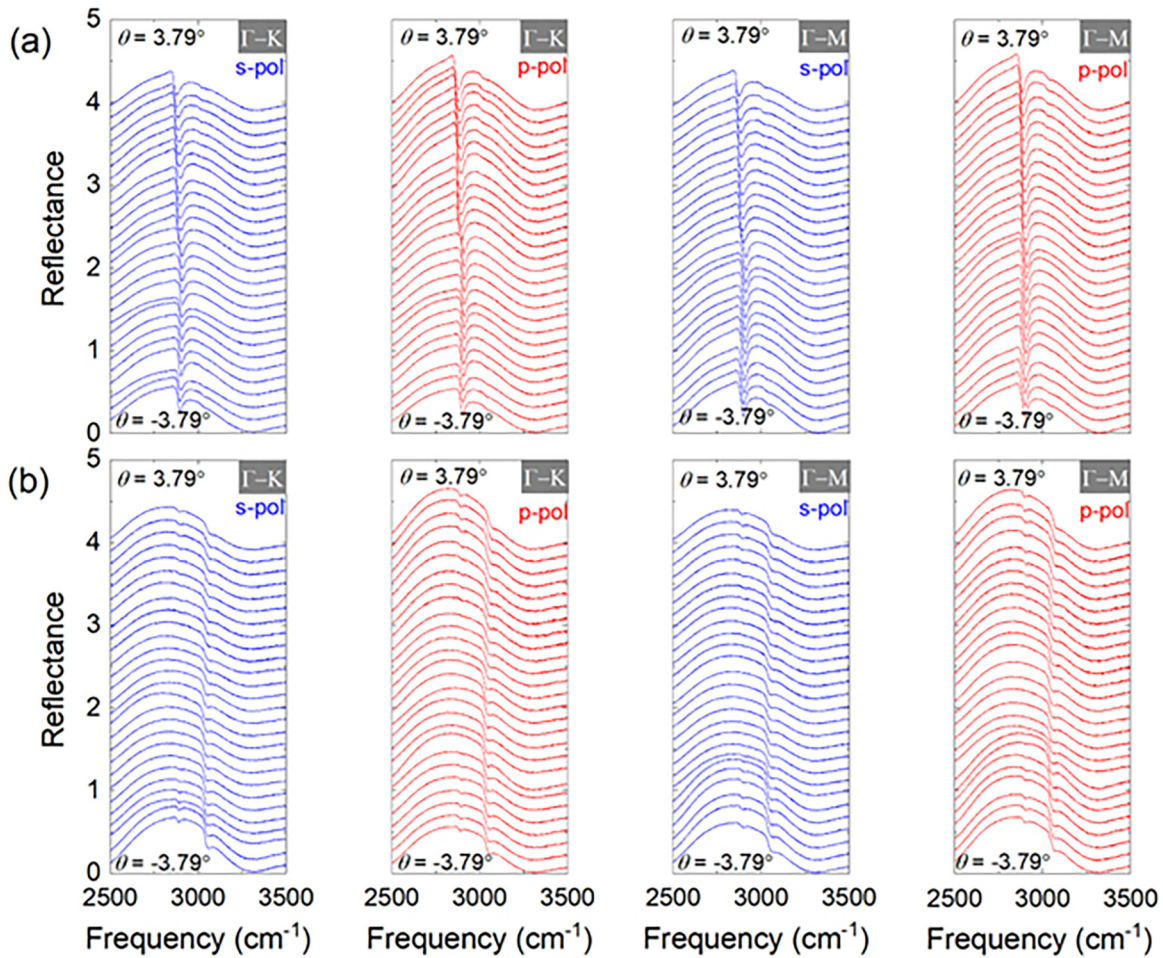
FIG. 6. Angle-resolved reflection spectra of (a) PhC-t and (b) PhC-n. The reflection spectra were measured by our homemade high-resolution setup from incident angles (θ) $-3.79°$ to $3.79°$. The incident beam was tilted to the Γ-to-K and Γ-to M directions with s and p polarizations. Twenty-seven spectra were measured for different incident angles in $0.292°$ steps. In each panel, the upper and lower limits of the lowest reflection spectrum are 1 and 0, respectively. Other spectra are drawn in the same scale and shifted by 0.15 in the vertical direction.

two PhCs by the bulk-edge correspondence [6] as shown in Fig. 3.

B. Edge modes

Figure 8 shows the reflection spectra of the combination specimen for p and s polarizations. In each panel, two distinct Fano-type resonance peaks are observed around 2900 and 3050 cm^{-1}, which originate from the E_1 modes of PhC-t and PhC-n, respectively. In each spectrum, one small dip is also observed in the mid-gap frequency range in addition to a few dips in the lower frequency side ($\leqslant$2900 cm^{-1}) of the common band gap. The former originates from the lower (p polarization) and upper (s polarization) branches of the edge modes, whereas the latter originate from discretized bulk modes due to the periodic arrangements of PhC-t and PhC-n of 20 unit cells. The latter feature is not so distinct on the higher frequency side of the common band gap. Because the mid-gap dips for the s polarization were shallow and detectable only for small incident angles (θ), we plotted such reflection spectra for which the mid-gap dips were relatively distinct. The reason for the shallower dips for the s polarization is not clear at present, although they

may be caused by an interference between the edge-mode dip and the higher E_1-mode dip, the latter of which has a full width at half maximum larger than that of the lower E_1-mode dip.

To confirm the edge-mode dispersion relation, we extracted the eigenmode frequencies from the observed spectra by the following curve-fitting procedure (see Fig. 9). Because the reflection dips of the mid-gap modes were shallow, we first took the difference between the reflection spectrum of the combination specimen and the averaged spectrum of bulk PhC-t and PhC-n. By this procedure, we could emphasize the mid-gap mode to some extent, although we could not completely eliminate the E_1-mode dips or background undulations because the bulk states in the combination specimen are not exactly the same as those in PhC-t or PhC-n. Then, we performed the curve fitting with a combination of three functions, that is, a third-order polynomial for the background undulation and two asymmetric Lorentzian functions (Fano functions) for E_1-mode and mid-gap-mode dips. For s (p) polarization, the upper (lower) E_1 mode around 3050 cm^{-1} (2900 cm^{-1}) was taken into consideration in the curve fitting, since we anticipated that the mid-gap modes approach the upper (lower) E_1-mode frequency with increasing θ. The result
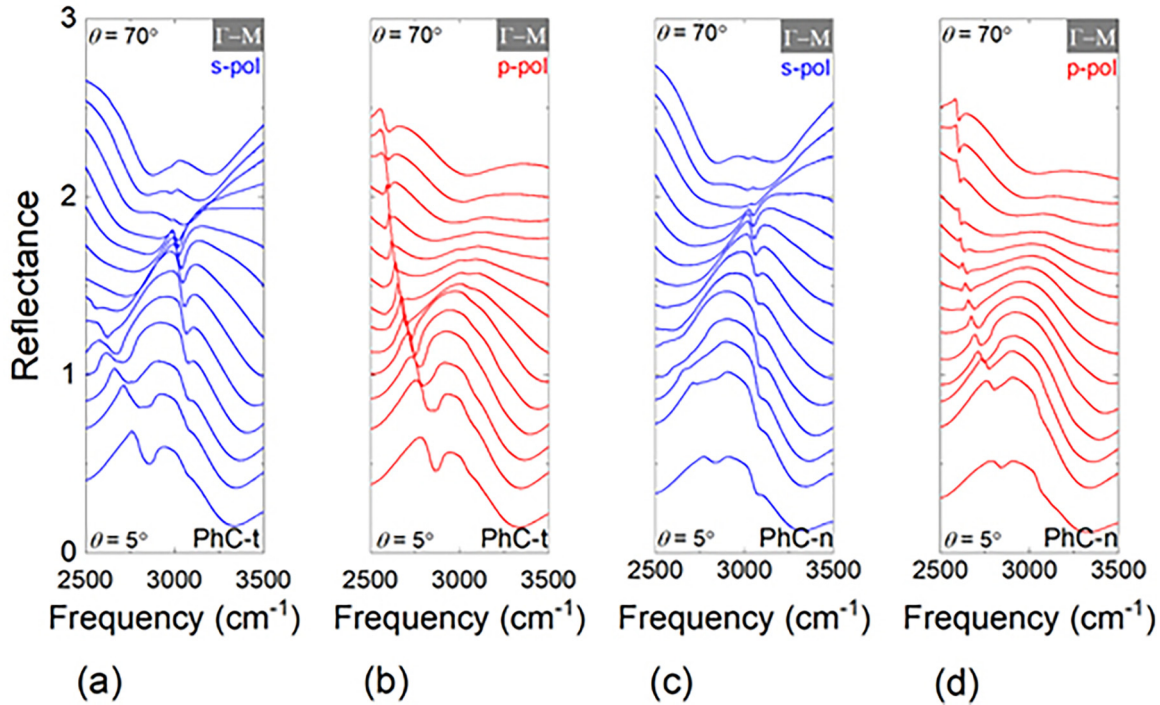
FIG. 7. Angle-resolved reflection spectra measured in the Γ-to-M direction for PhC-t [panels (a) and (b)] and PhC-n [panels (c) and (d)] for both s and p polarizations by the commercial variable-angle reflection accessory, Seagull. Each panel consists of 14 spectra measured for different incident angles (θ) in 5° steps. The upper and lower limits of the lowest reflection spectrum in each panel are 1 and 0, respectively. Other spectra are drawn in the same scale and shifted by 0.15 in the vertical direction.

of the curve fitting for s polarization and $\theta = 0°$ is presented in Fig. 9 as an example.

On the other hand, the E_1-mode frequencies of the edge-mode specimen or, more exactly, the gap-edge-mode frequencies were determined by curve fitting to the original reflection spectra because their spectra were large enough and the subtraction of the averaged spectra of PhC-t and PhC-n may result in a large spectral shift.

Now, we plotted the resonance frequencies of the p- and s-active mid-gap modes thus obtained against the lateral component of the incident wave vector in Fig. 10. In this figure, two gap-edge bulk-mode frequencies found in Fig. 8 are also plotted. Because there was a 28.3-cm^{-1} difference between calculated and observed E_1- and E_2-mode frequencies on average for PhC-t and PhC-n due to numerical and fabrication errors as shown in Sec. V A, this amount was subtracted from the observed frequencies. Then, Fig. 10 shows a good agreement between the observed and calculated dispersion relations for both edge modes and gap-edge modes. The discrepancy between the observed and calculated frequencies was smaller than 0.9% for the former and 2.0% for the latter. In addition, we should note that the lower (upper) branch of the edge modes is linearly polarized in the x (y) direction [p (s) polarized] in the vicinity of the Γ point due to a 1:1 mixture of right and left circular polarizations, which was confirmed by numerical analysis of their far-field pattern. Therefore, the above observation that the lower (upper) branch was p-active (s-active) is also consistent with our numerical calculation.

We make a remark here. Imperfections like air voids may cause the backscattering and/or additional diffractions of the edge modes. Although their precise evaluation is beyond the scope of the present study, we may estimate them by the spectral width of the edge-mode reflection dips. The observed spectral widths were larger than the calculated ones by approximately 50%, which implies the increase in the scattering and/or diffraction channels caused by the imperfections. However, the imperfections may include not only the defects but also the small number (20) of unit cells in the alignment direction of the trivial and nontrivial PhCs. So, the rigorous examination of this matter remains as a future problem.

VI. CONCLUSION

We presented a design of symmetric PhC slabs to materialize a complete photonic band gap for symmetric TE-like modes common to topologically trivial and nontrivial PhCs and revealed the presence of the topological edge modes on the boundary between the two PhCs. We successfully fabricated those PhC slabs by EB lithography of the top Si layer of SOI wafers and successive PECVD of a SiO$_2$ capping layer. The formation of the complete common band gap and the edge-mode dispersion were detected by angle-resolved reflection spectroscopy in the mid-IR range, which agreed well with numerical calculations. The common band gap was 3.1% wide experimentally and 4.1% wide theoretically, which is comparative to PhC membranes previously reported, although the refractive-index contrast of our specimens was considerably smaller than that of the PhC membranes.
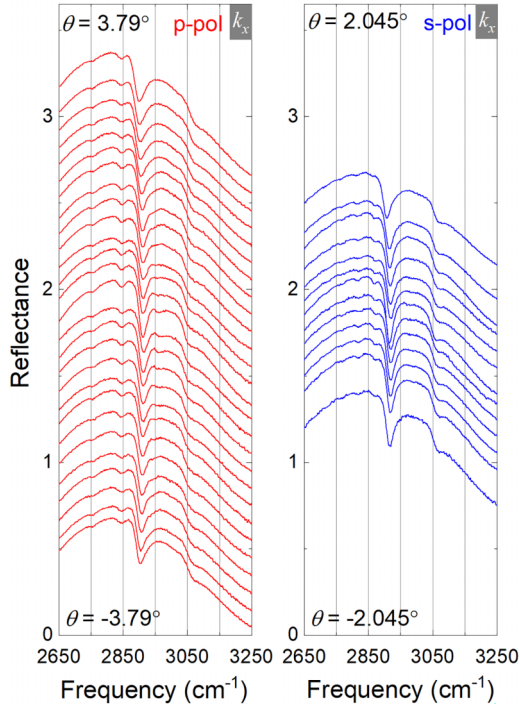
FIG. 8. Angle-resolved reflection spectra for the combination specimen of PhC-t and PhC-n of 20 unit cells each. The incident beam was tilted in the x direction (along the boundary between the two PhCs). For p polarization in the left panel, 27 spectra were measured for different incident angles in 0.292° steps from $\theta = -3.79°$ to 3.79°. The upper and lower limits of the lowest reflection spectrum are 1 and 0, respectively. Other spectra are drawn in the same scale and shifted by 0.1 in the vertical direction. For s polarization in the right panel, 13 spectra were measured from $\theta = -2.045°$ to 2.045° in 0.292° steps. The spectra were shifted by the same amount for each incident angle as in the left panel.

APPENDIX

Because PhC waveguide modes are confined in and around the top Si layer of SOI wafers, the influence of outer regions, that is, the Si substrate below the PhC and the air above the PhC, is negligible when the SiO$_2$ cladding and capping layers are sufficiently thick. To demonstrate this property, we examined the influence of the Si substrate as an example. For this purpose, we calculated the dispersion relation of the Si planar waveguide in the geometry of Figs. 11(a) and 11(b) to show that their dispersion relations are practically the same when the thickness of the SiO$_2$ cladding layer is 2 μm or larger.

In what follows, we assume that the air and SiO$_2$ layers in Fig. 11(a) and the air layer and the Si substrate in Fig. 11(b) are infinitely thick for simplicity. For the SiO$_2$ cladding layer in Fig. 11(b), we assume that it is 2 μm thick.

For the three-layer model, the secular equation for the TE polarization is given by

$$k_z(\gamma_1 + \gamma_3)\cos k_z d_2 - (k_z^2 - \gamma_1\gamma_3)\sin k_z d_2 = 0, \quad \text{(A1)}$$
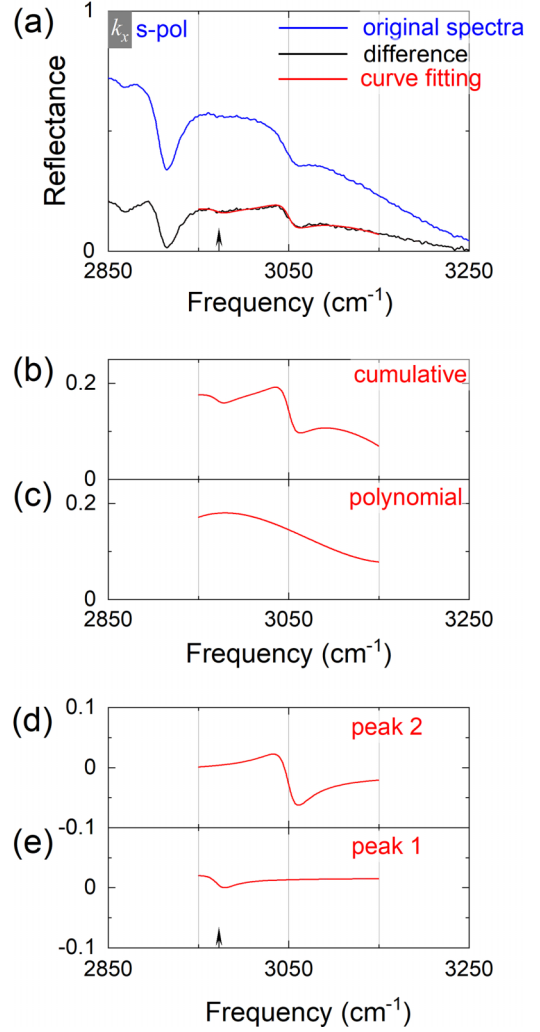
FIG. 9. An example of the curve-fitting procedure (s polarization, $\theta = 0°$). (a) Blue line: Original reflection spectrum of the combination specimen. Black line: Difference spectrum after subtracting the average of bulk PhC-t and PhC-n spectra at $\theta = 0°$. Red line: Result of the curve fitting. Arrows on the horizontal axis denote the resonance frequency obtained by the curve fitting. (b) Magnified view of the fitted curve, and (c)–(e) its three components.

which was obtained from the Maxwell wave equation and the natural boundary conditions. In Eq. (A1), d_2 is the thickness of the Si layer. γ_1 and γ_3 denote the spatial decay rates in the z direction in the air and SiO$_2$ layers, respectively, and k_z is the propagation constant in the z direction in the Si layer; these values are given as follows:

$$\gamma_1 = \sqrt{k^2 - \frac{\varepsilon_1 \omega^2}{c^2}}, \quad \text{(A2)}$$

$$k_z = \sqrt{\frac{\varepsilon_2 \omega^2}{c^2} - k^2}, \quad \text{(A3)}$$

$$\gamma_3 = \sqrt{k^2 - \frac{\varepsilon_3 \omega^2}{c^2}}, \quad \text{(A4)}$$

where ω is the eigenfrequency of the waveguide mode, k is its wave number in the x-y plane, and ε_i ($i = 1, 2,$ and 3) is the
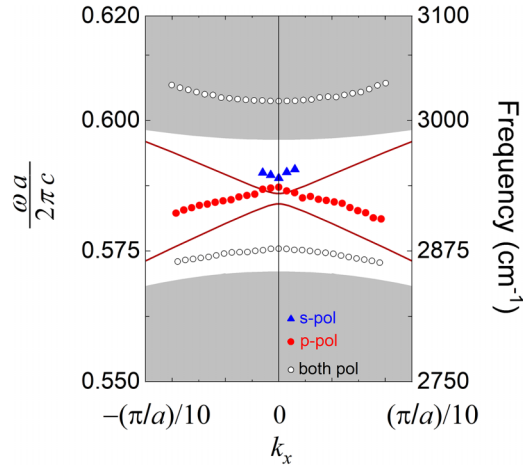
FIG. 10. Enlarged view of the edge-mode dispersion relation (maroon solid line) and the frequency range of the bulk modes (gray color) [Fig. 3(b)] together with mid-gap-mode frequencies (red closed circles are for *p*-active modes and blue closed triangles are for *s*-active modes) and gap-edge-mode frequencies (open circles) found in Fig. 8.

dielectric constant of each layer. We solved Eq. (A1) by the bisection method, assuming all ε_i were real.

On the other hand, we dealt with the same problem in the four-layer model in Fig. 11(b) by assuming a finite thickness for the SiO$_2$ cladding layer. In this case, the secular equation is given by

$$
\begin{aligned}
f(\omega, k) = (\gamma_3 + \gamma_4)e^{2\gamma_3 d_3}&\big\{(\gamma_1 + \gamma_2)(\gamma_2 + \gamma_3)e^{2\gamma_2 d_2} \\
&+ (\gamma_1 - \gamma_2)(\gamma_2 - \gamma_3)\big\} \\
+ (\gamma_3 - \gamma_4)&\big\{(\gamma_1 + \gamma_2)(\gamma_2 - \gamma_3)e^{2\gamma_2 d_2} \\
&+ (\gamma_1 - \gamma_2)(\gamma_2 + \gamma_3)\big\} \\
= 0.&
\end{aligned} \tag{A5}
$$

In Eq. (A5),

$$
\gamma_2 = \sqrt{k^2 - \frac{\varepsilon_2 \omega^2}{c^2}}, \tag{A6}
$$

$$
\gamma_4 = \sqrt{k^2 - \frac{\varepsilon_4 \omega^2}{c^2}}, \tag{A7}
$$

where ε_4 and γ_4 are the dielectric constant and the decay rate in the z direction of the Si substrate. d_3 denotes the thickness of the SiO$_2$ cladding layer. Equation (A5) was also derived from the Maxwell wave equation and the natural boundary conditions. Note that all waveguide modes are virtual modes
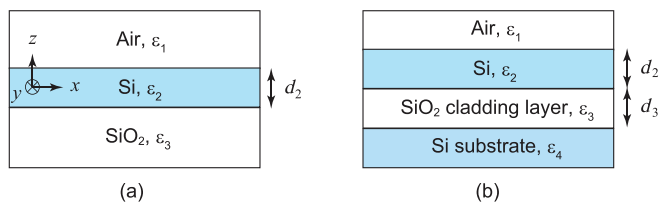
FIG. 11. (a) Three-layer and (b) four-layer models for the calculation of the dispersion relation of the Si planar waveguide.
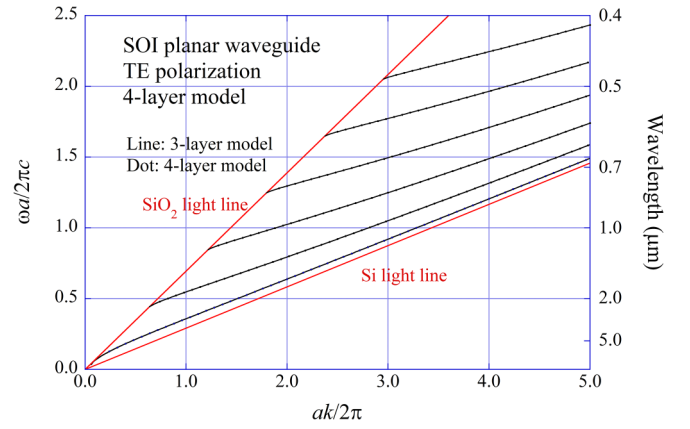
FIG. 12. Comparison of the three- and four-layer models. Black lines: Dispersion relation of TE modes calculated by the three-layer model. Blue dots: Eigenfrequency calculated by the four-layer model. The horizontal and vertical axes denote the dimensionless wave vector and the frequency normalized with the light velocity c and a length unit $a = 1$ μm. $\varepsilon_{\mathrm{Si}} = 11.74$, $\varepsilon_{\mathrm{SiO_2}} = 2.074$, $d_2 = 400$ nm, and $d_3 = 2.0$ μm. Note that the eigenfrequency for the four-layer model is complex and its real part is plotted.

for the four-layer model because they can escape to the Si substrate across the SiO$_2$ layer, although the escape rate may be low. This feature is represented by imaginary γ_2 and γ_4, and the eigenfrequency obtained by the four-layer model is generally complex. So, the bisection method is not applicable. We solved Eq. (A5) by a complex contour integral as described below.

When we derive the dispersion relation of the planar waveguide modes, we first specify the value of k and calculate the corresponding ω. When the eigenvalue is nondegenerate, which is the usual case for the planar waveguide dispersion, we can find the solution of Eq. (A5), ω_k, by the following contour integral in the complex ω plane based on the residue theorem:

$$
\omega_k = \frac{1}{2\pi i} \oint_C d\omega \frac{\omega f'(\omega, k)}{f(\omega, k)}, \tag{A8}
$$

where prime means differentiation with respect to ω and contour C encloses ω_k in the complex ω plane. This equation can be verified by the Taylor expansion of $f(\omega, k)$ around ω_k. We need the first guess of ω_k to set the contour, for which the solution of the three-layer model can be used, for example. Once the first solution has been obtained, we may gradually change k to calculate the dispersion by setting contour C to enclose the latest solution.

The dispersion curves calculated by both three-layer and four-layer models are shown in Fig. 12, where the former results are represented by black lines and the latter results are denoted by blue dots. Their agreement is pretty good, which means that the influence of the Si substrate on the dispersion relation is negligible when the SiO$_2$ cladding layer is 2 μm or thicker.

[1] C. L. Kane and E. J. Mele, Quantum Spin Hall Effect in Graphene, Phys. Rev. Lett. **95**, 226801 (2005).

[2] B. A. Bernevig, T. L. Hughes, and S.-C. Zhang, Quantum spin Hall effect and topological phase transition in HgTe quantum wells, Science **314**, 1757 (2006).

[3] D. Hsieh, D. Qian, L. Wray, Y. Xia, Y. S. Hor, R. J. Cava, and M. Z. Hasan, A topological Dirac insulator in a quantum spin Hall phase, Nature (London) **452**, 970 (2008).

[4] M. Z. Hasan and C. L. Kane, Colloquium: Topological insulators, Rev. Mod. Phys. **82**, 3045 (2010).

[5] X.-L. Qi and S.-C. Zhang, Topological insulators and superconductors, Rev. Mod. Phys. **83**, 1057 (2011).

[6] L. H. Wu and X. Hu, Scheme for Achieving a Topological Photonic Crystal by Using Dielectric Material, Phys. Rev. Lett. **114**, 223901 (2015).

[7] S. Barik, A. Karasahin, C. Flower, T. Cai, H. Miyake, W. DeGottardi, M. Hafezi, and E. Waks, A topological quantum optics interface, Science **359**, 666 (2018).

[8] S. Barik, H. Miyake, W. DeGottardi, E. Waks, and M. Hafezi, Two-dimensionally confined topological edge states in photonic crystals, New J. Phys. **18**, 113013 (2016).

[9] N. Parappurath, F. Alpeggiani, L. Kuipers, and E. Verhagen, Direct observation of topological edge states in silicon photonic crystals: Spin, dispersion, and chiral routing, Sci. Adv. **6**, eaaw4137 (2020).

[10] A. M. Dubrovkin, U. Chattopadhyay, B. Qiang, O. Buchnev, Q. J. Wang, Y. Chong, and N. I. Zheludev, Near-field mapping of the edge mode of a topological valley slab waveguide at $\lambda = 1.55\ \mu\mathrm{m}$, Appl. Phys. Lett. **116**, 191105 (2020).

[11] S. Arora, T. Bauer, R. Barczyk, E. Verhagen, and L. Kuipers, Direct quantification of topological protection in symmetry-protected photonic edge states at telecom wavelengths, Light: Sci. Appl. **10**, 9 (2021).

[12] S. Shamim, W. Beugeling, P. Shekhar, K. Bendias, L. Lunczer, J. Kleinlein, H. Buhmann, and L. W. Molenkamp, Quantized spin Hall conductance in a magnetically doped two-dimensional topological insulator, Nat. Commun. **12**, 3193 (2021).

[13] C. Liu, D. Culcer, Z. Wang, M. T. Edmonds, and M. S. Fuhrer, Helical edge transport in millimeter-scale thin films of Na$_3$B, Nano Lett. **20**, 6306 (2020).

[14] J. A. Vaitkus, C. S. Ho, and J. H. Cole, Effect of magnetic impurity scattering on transport in topological insulator, Phys. Rev. B **106**, 115420 (2022).

[15] M. McGinley and N. R. Cooper, Elastic backscattering of quantum spin Hall edge modes from Coulomb interactions with nonmagnetic impurities, Phys. Rev. B **103**, 235164 (2021).

[16] B. Orazbayev and R. Fleury, Quantitative robustness analysis of topological edge modes in C6 and valley-Hall metamaterial waveguides, Nanophotonics **8**, 1433 (2019).

[17] B. Bradlyn, L. Elcoro, J. Cano, M. G. Vergniory, Z. Wang, C. Felser, M. I. Aroyo, and B. A. Bernevig, Topological quantum chemistry, Nature (London) **547**, 298 (2017).

[18] L. Elcoro, B. J. Wieder, Z. Song, Y. Xu, B. Bradlyn, and B. A. Bernevig, Magnetic topological quantum chemistry, Nat. Commun. **12**, 5965 (2021).

[19] M. Lončar, D. Nedeljković, T. Doll, J. Vučković, A. Scherer, and T. P. Pearsall, Waveguiding in planar photonic crystals, Appl. Phys. Lett. **77**, 1937 (2000).

[20] P. L. Gourley, J. R. Wendt, G. A. Vawter, T. M. Brennan, and B. E. Hammons, Optical properties of two-dimensional photonic lattices fabricated as honeycomb nanostructures in compound semiconductors, Appl. Phys. Lett. **64**, 687 (1994).

[21] M. Kanskar, P. Paddon, V. Pacradouni, R. Morin, A. Busch, J. F. Young, S. R. Johnson, J. Mackenzie, and T. Tiedje, Observation of leaky slab modes in an air-bridged semiconductor waveguide with a two-dimensional photonic lattice, Appl. Phys. Lett. **70**, 1438 (1997).

[22] S. Fan, P. R. Villeneuve, J. D. Joannopoulos, and E. F. Schubert, High Extraction Efficiency of Spontaneous Emission from Slabs of Photonic Crystals, Phys. Rev. Lett. **78**, 3294 (1997).

[23] D. Labilloy, H. Benisty, C. Weisbuch, T. F. Krauss, R. M. De La Rue, V. Bardinal, R. Houdré, U. Oesterle, D. Cassagne, and C. Jouanin, Quantitative Measurement of Transmission, Reflection, and Diffraction of Two-Dimensional Photonic Band Gap Structures at Near-Infrared Wavelengths, Phys. Rev. Lett. **79**, 4147 (1997).

[24] B. D'Urso, O. Painter, J. O'Brien, T. Tombrello, A. Yariv, and A. Scherer, Modal reflectivity in finite-depth two-dimensional photonic-crystal microcavities, J. Opt. Soc. Am. B **15**, 1155 (1998).

[25] D. Labilloy, H. Benisty, C. Weisbuch, C. J. M. Smith, T. F. Krauss, R. Houdré, and U. Oesterle, Finely resolved transmission spectra and band structure of two-dimensional photonic crystals using emission from InAs quantum dots, Phys. Rev. B **59**, 1649 (1999).

[26] O. Painter, R. K. Lee, A. Scherer, A. Yariv, J. D. O'Brien, P. D. Dapkus, and I. Kim, Two-dimensional photonic band-gap defect mode laser, Science **284**, 1819 (1999).

[27] S. G. Johnson, S. Fan, P. R. Villeneuve, J. D. Joannopoulos, and L. A. Kolodziejski, Guided modes in photonic crystal slabs, Phys. Rev. B **60**, 5751 (1999).

[28] S. Kuchinsky, D. C. Allan, N. F. Borrelli, and J. C. Cotteverte, 3D localization in a channel waveguide in a photonic crystal with 2D periodicity, Opt. Commun. **175**, 147 (2000).

[29] T. Kuroda, N. Ikeda, T. Mano, Y. Sugimoto, T. Ochiai, K. Kuroda, S. Ohkouchi, N. Koguchi, K. Sakoda, and K. Asakawa, Acceleration and suppression of photoemission of GaAs quantum dots embedded in photonic crystal microcavities, Appl. Phys. Lett. **93**, 111103 (2008).

[30] M. Aspelmeyer, T. J. Kippenberg, and F. Marquardt, Cavity optomechanics, Rev. Mod. Phys. **86**, 1391 (2014).

[31] H. Ren, M. H. Matheny, G. S. MacCabe, J. Luo, H. Pfeifer, M. Mirhosseini, and O. Painter, Two-dimensional optomechanical crystal cavity with high quantum cooperativity, Nat. Commun. **11**, 3373 (2020).

[32] K. Sakoda, *Optical Properties of Photonic Crystals*, 2nd ed. (Springer, Berlin, 2004).

[33] D. Chandler-Horowitz and P. M. Amirtharaj, High-accuracy, midinfrared ($450\ \mathrm{cm}^{-1} \leqslant \omega \leqslant 4000\ \mathrm{cm}^{-1}$) refractive index values of silicon, J. Appl. Phys. **97**, 123526 (2005).

[34] I. H. Malitson, Interspecimen comparison of the refractive index of fused silica, J. Opt. Soc. Am. **55**, 1205 (1965).

[35] S. Chalimah, Y. Yao, N. Ikeda, Y. Sugimoto, T. Mano, T. Kuroda, and K. Sakoda, Eigenmode symmetry assignment of

triangular-lattice photonic crystal slabs and their Dirac cone materialized by effective degeneracy in the mid-infrared region, Opt. Express **29**, 19486 (2021).

[36] A. Begum, Y. Yao, T. Kuroda, Y. Takeda, N. Ikeda, Y. Sugimoto, T. Mano, and K. Sakoda, Design and observation of topological bandgaps and edge modes in SOI photonic crystal slabs (unpublished).

[37] S. Chalimah, Y. Yao, N. Ikeda, K. Kaneko, R. Hashimoto, T. Kakuno, S. Saito, T. Kuroda, Y. Sugimoto, and K. Sakoda, Mid-Infrared Dispersion Relations in InP-Based Photonic Crystal Slabs revealed by Fourier-Transform Angle-Resolved Reflection Spectroscopy, Phys. Rev. Appl. **15**, 064076 (2021).

[38] A. Begum, Y. Yao, T. Kuroda, E. Watanabe, N. Ikeda, Y. Sugimoto, Y. Takeda, and K. Sakoda, Observation of two-dimensional isotropic double Dirac cones in the electromagnetic dispersion relation, J. Phys. Soc. Jpn. **91**, 084401 (2022).

[39] T. Kuroda, S. Chalimah, Y. Yao, N. Ikeda, Y. Sugimoto, and K. Sakoda, Apparatus for high-precision angle-resolved reflection spectroscopy in mid-infrared region, Appl. Spectrosc. **75**, 259 (2021).